

## A HIGHER EFFICIENCY OF CONVERTING GAS TO STARS PUSH GALAXIES AT $Z \sim 1.6$ WELL ABOVE THE STAR-FORMING MAIN SEQUENCE

J. D. SILVERMAN<sup>1</sup>, E. DADDI<sup>2</sup>, G. RODIGHIERO<sup>3</sup>, W. RUJOPAKARN<sup>1,4</sup>, M. SARGENT<sup>5</sup>, A. RENZINI<sup>6</sup>, D. LIU<sup>2</sup>, C. FERUGLIO<sup>7</sup>, D. KASHINO<sup>6</sup>, D. SANDERS<sup>9</sup>, J. KARTALTEPE<sup>10</sup>, T. NAGAO<sup>11</sup>, N. ARIMOTO<sup>12</sup>, S. BERTA<sup>13</sup>, M. BÉTHÉRMIN<sup>14</sup>, D. LUTZ<sup>13</sup>, G. MAGDIS<sup>15,16</sup>, C. MANCINI<sup>6</sup>, M. ONODERA<sup>17</sup>, G. ZAMORANI<sup>18</sup>

*Submitted to The Astrophysical Journal Letters*

### ABSTRACT

Local starbursts have a higher efficiency of converting gas into stars, as compared to typical star-forming galaxies at a given stellar mass, possibly indicative of different modes of star formation. With the peak epoch of galaxy formation occurring at  $z > 1$ , it remains to be established whether such an efficient mode of star formation is occurring at high-redshift. To address this issue, we measure the CO molecular gas content of seven high-redshift ( $z \sim 1.6$ ) starburst galaxies with ALMA and IRAM/PdBI. Our sample is selected from the FMOS-COSMOS near-infrared spectroscopic survey of star-forming galaxies at  $z \sim 1.6$  with Subaru. All galaxies have star formation rates ( $\sim 300\text{--}800 M_{\odot} \text{ yr}^{-1}$ ) elevated ( $\gtrsim 4\times$ ) above the star-forming main sequence. We detect CO emission in all cases at high significance, indicative of plentiful gas supplies ( $f_{gas} \sim 30\text{--}50\%$ ). Even more compelling, we firmly establish for the first time that starbursts at high redshift systematically have a lower ratio of CO to total infrared luminosity as compared to typical ‘main-sequence’ star-forming galaxies, although with an offset less than expected based on past studies of local starbursts. We put forward a hypothesis that there exists a continuous increase in star formation efficiency with elevation from the main sequence with galaxy mergers as a possible physical driver. Along with a heightened star formation efficiency, our high-redshift sample is similar in other respects to local starbursts such as being metal rich and having a higher ionisation state of the ISM.

*Keywords:* galaxies: ISM — galaxies: high-redshift — galaxies: starburst — galaxies: star formation

### 1. INTRODUCTION

It has recently come to light that the growth of galaxies may be less erratic than previously thought. The existence of a tight relation between the stellar mass ( $M_{*}$ ) and the star formation rate (SFR) of star-forming galaxies, termed the ‘main sequence’ (MS, Noeske et al. 2007; Daddi et al. 2007; Elbaz et al. 2007; Whitaker et al. 2012; Kashino et al. 2013; Speagle et al. 2014) is indicative of a quasi-equilibrium being maintained between gas supply, SFR, and gas expulsion from galaxies (e.g., Bouché et al. 2010; Lilly et al. 2013). This SFR- $M_{*}$  relation evolves strongly with look-back time, paralleling the global evolution of the cosmic SFR density from the present to  $z \sim 2$  (Madau & Dickinson 2014). It is becoming clear that such a decline in SFR is in response to diminishing gas reservoirs (e.g., Tacconi et al. 2013; Scoville et al. 2014; Santini et al. 2014). The efficiency of star formation ( $SFE \equiv SFR/M_{gas}$ ), i.e., the efficiency at which gas is being converted to stars, is remarkably similar across a wide range of cosmic time within the global star-forming population, usually with gas mass  $M_{gas}$  inferred from the CO molecular line luminosity  $L_{CO}$  (e.g., Tacconi et al. 2010, 2013; Daddi et al. 2010b).

However, outliers from the MS are also known to exist, with very high specific SFR (sSFR) compared to normal MS galaxies, such as local ultra-luminous infrared galaxies (ULIRG, Sanders & Mirabel 1996). At  $z \sim 2$ , these MS outliers represent  $\sim 2\%$  of the global star-forming population and contribute only a moderate

Electronic address: john.silverman@ipmu.jp

<sup>1</sup> Kavli Institute for the Physics and Mathematics of the Universe, Todai Institutes for Advanced Study, the University of Tokyo, Kashiwa, Japan 277-8583 (Kavli IPMU, WPI)

<sup>2</sup> Laboratoire AIM, CEA/DSM-CNRS-Université Paris Diderot, Irfu/Service d’Astrophysique, CEA Saclay

<sup>3</sup> Dipartimento di Fisica e Astronomia, Università di Padova, vicolo Osservatorio, 3, 35122, Padova, Italy

<sup>4</sup> Department of Physics, Faculty of Science, Chulalongkorn University, 254 Phayathai Road, Pathumwan, Bangkok 10330, Thailand

<sup>5</sup> Astronomy Centre, Department of Physics and Astronomy, University of Sussex, Brighton, BN1 9QH, UK

<sup>6</sup> Istituto Nazionale de Astrofisica, Osservatorio Astronomico di Padova, v.co dell’Osservatorio 5, I-35122, Padova, Italy, EU

<sup>7</sup> IRAM - Institut de RadioAstronomie Millimétrique, 300 rue de la Piscine, 38406 Saint Martin d’Hères, France

<sup>8</sup> Division of Particle and Astrophysical Science, Graduate School of Science, Nagoya University, Nagoya, 464-8602, Japan

<sup>9</sup> Institute for Astronomy, University of Hawaii, 2680 Woddlawn Drive, Honolulu, HI, 96822

<sup>10</sup> National Optical Astronomy Observatory, 950 N. Cherry Ave., Tucson, AZ, 85719

<sup>11</sup> Graduate School of Science and Engineering, Ehime University, 2-5 Bunkyo-cho, Matsuyama 790-8577, Japan

<sup>12</sup> Subaru Telescope, 650 North A’ohoku Place, Hilo, Hawaii, 96720, USA

<sup>13</sup> Max-Planck-Institut für extraterrestrische Physik, D-84571 Garching, Germany

<sup>14</sup> European Southern Observatory, Karl-Schwarzschild-Str. 2, 85748 Garching, Germany

<sup>15</sup> Department of Physics, University of Oxford, Keble Road, Oxford OX1 3RH, UK

<sup>16</sup> Institute for Astronomy, Astrophysics, Space Applications and Remote Sensing, National Observatory of Athens, GR-15236 Athens, Greece

<sup>17</sup> Institute of Astronomy, ETH Zürich, CH-8093, Zürich, Switzerland

<sup>18</sup> INAF Osservatorio Astronomico di Bologna, via Ranzani 1,

I-40127, Bologna, Italy

fraction ( $\sim 10\%$ ) of the global co-moving SFR-density (Rodighiero et al. 2011). Yet, they are still likely to play an important role in galaxy evolution, as a high fraction of galaxies may experience such a star-bursting event. Therefore, it is important to understand the physical conditions that can lead to such a surge in SFR in previously normal star-forming galaxies.

Local starbursts operate with a higher SFE compared to MS galaxies. Estimates of their molecular gas content from their CO luminosity indicate that a given gas mass is capable of producing higher SFRs (Solomon et al. 1997), and a bi-modal distribution of SFEs has been proposed for the general MS and outlier population (Daddi et al. 2010b; Genzel et al. 2010). While there are uncertainties with respect to the appropriate conversion of  $L_{\text{CO}}$  to  $\text{H}_2$  gas mass ( $\alpha_{\text{CO}}$ ), an offset with respect to MS galaxies is apparent when considering the observed quantities  $L_{\text{CO}}$  and total infrared luminosity ( $L_{\text{TIR}}$ ). The physical mechanism(s) responsible for this enhanced SFE is not entirely clear and one cannot exclude that sample selection may be responsible for the lack of galaxies with intermediate SFEs. While CO detections have been obtained for high-redshift submm-selected galaxies (SMGs; e.g., Swinbank et al. 2014), the sample does not distinguish between starburst outliers from MS galaxies. Therefore, it is imperative to build a larger sample of ‘typical’ starbursts near the peak epoch ( $z \sim 2$ ) of star formation.

To address this issue, we report on interferometric observations of the molecular transition CO 2-1 and CO 3-2 for a sample of seven MS outliers using both Atacama Large Millimeter Array (ALMA) and IRAM Plateau de Bure Interferometer. Our galaxy sample is extracted from the 150 MS outliers (with sSFRs  $\gtrsim 4\times$  above the mean of the MS; Figure 1) at  $1.5 < z < 2.5$  identified with Herschel observations over the COSMOS field (Rodighiero et al. 2011). Among these Herschel-detected galaxies, those with photometric redshifts between 1.4 and 1.7 are observed through our Subaru Intensive Project (Silverman et al. 2014) with the FMOS near-IR multi-object spectrograph. These spectra provide a detection of key diagnostic emission lines (i.e.,  $\text{H}\alpha$ ,  $\text{H}\beta$ ,  $[\text{NII}]\lambda 6585$ ,  $[\text{OIII}]\lambda 5008$ ) used to measure accurate spectroscopic redshifts, SFRs, and metallicities. Six targets, labeled in Figure 1, are extracted from this sample with an additional galaxy at a slightly higher redshift (PACS-282;  $z = 2.19$ ) where the redshift comes from the zCOSMOS-Deep program (Lilly et al. 2007).

Our confidence in these galaxies being ‘outliers’ in the SFR– $M_*$  plane is based on the exquisite multi-wavelength coverage of the COSMOS field. Stellar masses are derived from SED-fitting using Hyperz with stellar population synthesis models (Bruzual & Charlot 2003) at the respective spectroscopic redshift. The deblending of detections in Herschel (or  $70\mu\text{m}$  *Spitzer*) images relies upon *Spitzer* MIPS  $24\mu\text{m}$  priors. SFRs are derived from  $L_{\text{TIR}}$ , an integral of the SED from the mid-to-far-IR (24 - 500  $\mu\text{m}$ ) using Herschel PACS and SPIRE bands, thus accounting for the obscured star formation as in Magdis et al. (2012). Moreover, four of the seven galaxies have 1.4 GHz radio detections at  $> 5\sigma$  level (Schinnerer et al. 2010) and radio-based SFRs are consistent with being above the MS. Throughout this work, we assume  $H_0 = 70 \text{ km s}^{-1} \text{ Mpc}^{-1}$ ,  $\Omega_\Lambda = 0.7$ ,  $\Omega_M = 0.3$ ,

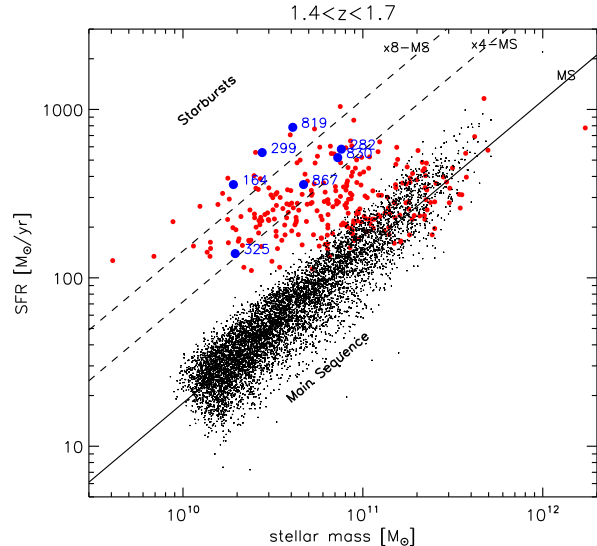


**Figure 1.** SFR versus  $M_*$  for galaxies with  $1.4 < z < 1.7$  in COSMOS. Galaxies with CO observations are shown in blue. For reference, we plot star-forming galaxies that denote the MS (small dots). *Herschel*-detected galaxies include our sample in blue and those shown in red.

and use a Salpeter IMF for SFRs and stellar masses.

## 2. OBSERVATIONS OF CO EMISSION AT HIGH-Z

ALMA observations of five galaxies using 34 12m antennas and the band 3 receiver (centered near 90 GHz) were carried out in Cycle 1 (Project 2012.1.00952.S). Two ‘scheduling blocks’ (SB1 and SB2) were defined to accommodate the requirements to detect CO 2-1 within a single sideband (2 GHz width) for each of our targets (SB1: PACS- 819, 830; SB2: PACS- 325, 299 and 867). We required exposure times sufficient to reach a flux sensitivity level of 0.2 mJy (SB1) and 0.1 mJy (SB2) per target with the aim to measure the total unresolved CO emission. It was estimated that the integrated line detection would have a significance of  $5\sigma$  based on predictions of CO emission from their IR luminosity and an assumed ratio  $L_{\text{CO}}/L_{\text{TIR}}$  ( $3\times$  lower than MS galaxies). Our observations were carried out with baselines resulting in a beam size of  $\sim 5 - 6''$  for three cases (PACS 325, 299 and 867) and  $\lesssim 1''$  for PACS-819 and PACS-830.

We measure the CO flux by fitting the data in UV space with the GILDAS task ‘uvfit’ in the MAPPINGS package. The fit was performed using a circular Gaussian that returns the centroid, de-convolved source size, and integrated flux. We find good agreement between fluxes returned from GILDAS with those using ‘imfit’ in the image plane with CASA, after resolving software issues on exporting the ALMA data to a GILDAS-compatible format. Additionally, we resolve the emission for PACS-819 and 830; therefore, a measure of the source extent is reported.

To increase the sample size, interferometric measurements were obtained with IRAM/PdBI for PACS-282 (CO 3-2) and PACS-164 (CO 2-1). For PACS-282 (PACS-164), an integration time of 6.2 (12.9) hours, using the 3mm band in configuration D, was achieved that resulted in a limiting  $1\sigma$  sensitivity level of 0.13 (0.11) mJy beam $^{-1}$ . CO fluxes are measured with GILDAS as for the ALMA data. In Table 1, we list the source

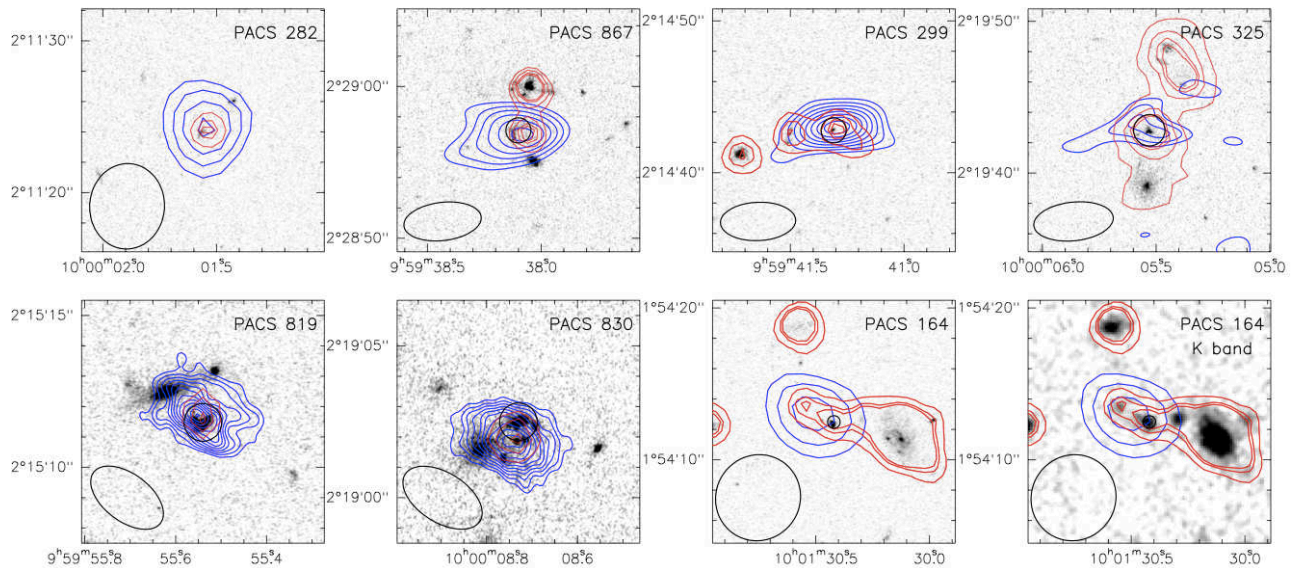


**Figure 2.** HST/ACS F814W images of our seven starbursts. CO emission is shown as contours in blue starting at  $3\sigma$  and in steps of  $1\sigma$  above the rms noise level. *Spitzer*/IRAC  $3.6\mu\text{m}$  detections are marked with red contours to illustrate the association of peak CO emission with their IR counterparts. CO beam size is indicated in the lower left corner. Small black circles show the placement of FMOS fibers. For PACS-164 the *K*-band image is shown to illustrate, in comparison with the HST image, the heavily-obscured nature of the CO-emitting region. The angular size of the cutouts can vary.

**Table 1**  
Sample data and CO measurements<sup>a</sup>

PACS ID	RA (CO)	Dec (CO)	$z_{CO}$	$z_{spec}$ <sup>b</sup>	$\log M_*$ $M_\odot$	SFR <sup>c</sup>	$I_{CO}$ $\text{Jy km s}^{-1}$	$L'_{CO}$ <sup>d</sup>	$\Delta v$ <sup>e</sup>	Beam <sup>f</sup> size ( $''$ )	CO size ( $''$ )	Gas <sup>g</sup> fraction
299	09:59:41.31	02:14:42.91	1.650	1.646	10.44	554	$0.67 \pm 0.08$	10.44	590	$4.5 \times 2.0$	$< 2.4$	0.52
325	10:00:05.47	02:19:42.61	1.657	1.657	10.29	139	$0.28 \pm 0.06$	10.07	764	$5.4 \times 2.7$		0.32
819	09:59:55.55	02:15:11.70	1.444	1.445	10.61	783	$1.10 \pm 0.07$	10.55	592	$1.3 \times 1.0$	$0.34 \pm 0.08$	0.34
830	10:00:08.75	02:19:01.90	1.462	1.461	10.86	517	$1.18 \pm 0.10$	10.59	436	$1.3 \times 1.0$	$0.97 \pm 0.17$	0.46
867	09:59:38.12	02:28:56.56	1.567	1.567	10.67	358	$0.46 \pm 0.04$	10.24	472	$4.4 \times 2.0$	$< 1.5$	0.29
282	10:00:01.54	02:11:24.27	2.192	2.190	10.88	581	$0.75 \pm 0.12$	10.44	660	$5.6 \times 4.9$	$< 3.4$	0.28
164	10:01:30.53	01:54:12.96	1.647	1.650	$> 10.28$	358	$0.61 \pm 0.11$	10.40	894	$5.7 \times 5.5$	$< 4.8$	0.52

<sup>a</sup> The first five targets are observed with ALMA while the remaining two with PdBI.

<sup>b</sup> Spectroscopic redshifts are based on  $H\alpha$  with the exception of #282.

<sup>c</sup> Units of  $M_\odot \text{ yr}^{-1}$ .

<sup>d</sup> Log base 10; units of  $\text{K km s}^{-1} \text{ pc}^2$

<sup>e</sup> Velocity channel width of the CO line in units of  $\text{km s}^{-1}$ .

<sup>f</sup> FWHM

<sup>g</sup>  $f_{gas} = M_{gas}/(M_* + M_{gas})$

properties and CO measurements.

### 3. RESULTS

We detect CO emission in all seven targeted galaxies with integrated flux densities ( $I_{CO}$ ) ranging from 0.28 to  $1.18 \text{ Jy km s}^{-1}$ . All but one have a high level of significance ( $> 5\sigma$ ) and those resulting from ALMA observations are above the  $8\sigma$  level with the exception of PACS-325 ( $S/N = 4.7$ ). In Figure 2, we display the optical HST/ACS *i*-band image cutouts with CO and  $3.6\mu\text{m}$  emission overlaid as contours. Using a large beam for the majority of the sample, the CO emission is essentially unresolved with the exception of two observations taken at higher resolution ( $\sim 1''$ ). PACS-819 has half of the emission coming from a region of  $3.2 \pm 0.8 \text{ kpc}$ , while PACS-830 is more extended ( $9.0 \pm 1.6 \text{ kpc}$ ). This may suggest that there is diversity in the size distribution of molecular gas at high redshift, dissimilar to local starbursts (e.g., Scoville et al. 1989).

Upon close inspection of the maps in Figure 2, it is

evident that the centroid of the CO emission is not always coincident with the brightest regions of UV emission as seen in the HST/ACS image (i.e., PACS-164, PACS-830, PACS-867). This is likely evidence that a fair fraction of the star formation is obscured as supported by the improved alignment of the CO emission with the peak infrared emission detected by *Spitzer* in both the IRAC and MIPS channels, and clear association with highly significant radio emission at 1.4 GHz (Schinnerer et al. 2010).

We note that the Herschel far-IR (and possibly the CO) emission of PACS-164 is likely the sum of two separate components seen in the IRAC image. The peak of the CO emission, detected by IRAM, is located somewhat between two IR sources, as made particularly clear by the *K*-band image also shown in Figure 2, and slightly elongated possibly indicating a contribution from both sources. The FMOS spectrum that provides the redshift ( $z = 1.650$ ) refers to the western IR component that is co-spatial with the UV-bright source seen in the HST image.

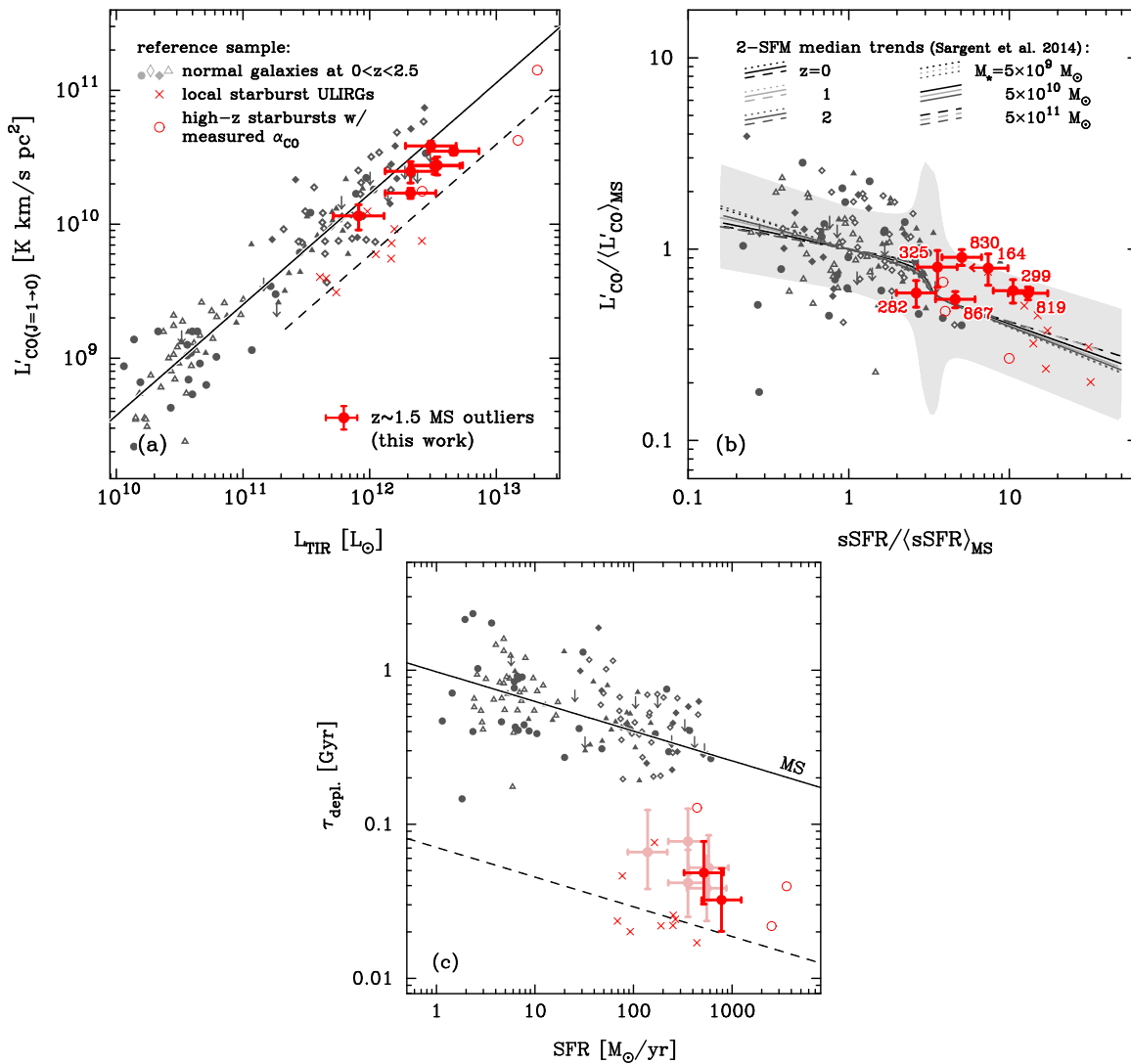


**Figure 3.** (a) CO luminosity versus total infrared luminosity. (b) CO luminosity and specific star formation rate with each normalized to the typical values of MS galaxies. Empirical model curves and  $1\sigma$  errors (grey region) are described in Sargent et al. (2014). (c) Gas depletion time ( $\tau_{\text{depl}} \equiv \text{SFE}^{-1}$ ; units Gyr) versus SFR. Colored symbols with error bars show our starburst sample with two (819 and 830) in bright red having dynamical mass measurements. Grey symbols represent published samples with  $\alpha_{\text{CO}}$  estimates as compiled in Sargent et al. (2014) and shown in all panels.

With a redshift of the CO emission ( $z = 1.647$ ) very close to that of the FMOS source, this system appears to be in the early stages of a merger given the projected separation of 18.7 kpc. The lower limit for the stellar mass of the system as reported in Table 1 refers to the mass of the object observed with FMOS, and encircled in Figure 2.

### 3.1. CO-to-IR ratio

Our primary interest is to determine whether high-redshift starbursts have a CO to IR luminosity ratio  $L'_{\text{CO}}/L_{\text{TIR}}$  dissimilar to that of MS galaxies at these epochs, which may be indicative of a higher efficiency of converting gas into stars, similar to that observed in local starbursts. To begin, we use observed quantities as opposed to derived values such as the gas mass surface density that relies on an assumed conversion factor of CO luminosity to  $\text{H}_2$  gas mass. Moreover, we do not have size information for our entire sample to measure the gas surface density. However, we note that

$L'_{\text{CO}}/L_{\text{TIR}} \sim M_{\text{gas}}/\text{SFR}$ , hence this luminosity ratio is a fair proxy for the gas depletion time which in turn is the inverse of the SFE.

In Figure 3a, we plot  $L'_{\text{CO}}$  as a function of  $L_{\text{TIR}}$ , indicative of the obscured SFR, and include both low- and high-redshift galaxies with measurements available in the literature and compiled in Sargent et al. (2014). All line luminosities are converted to CO 1-0 using values of 0.85 and 0.7, respectively for CO 2-1 and CO 3-2 (Daddi et al. 2015).

All galaxies in our sample have  $L'_{\text{CO}}/L_{\text{TIR}}$  below the well-established relation for MS galaxies. These observations indicate, for the first time, the existence of an offset in the  $L'_{\text{CO}}/L_{\text{TIR}}$  ratio for high-redshift starbursts as found by Solomon et al. (1997) for local ULIRGs. In Figure 3b, we plot these quantities, normalized to the mean value of galaxies on the MS. In addition, on the abscissa we replace  $L_{\text{TIR}}$  with its implied specific SFR ( $\text{sSFR} = \text{SFR}/M_*$ ), also normalized to the MS value. We measure the median value of  $L'_{\text{CO}} / \langle L'_{\text{CO}} \rangle_{\text{MS}} =$

$0.60 \pm 0.04$  for our sample. This represents an offset ( $1.7 \pm 0.1\times$ ) from the MS that is smaller than in local samples of starbursts ( $\sim 3\times$ ; dashed line in Fig. 3a). Along these lines, the starbursts in our sample have higher  $L'_{CO}$  than expected by  $\sim 0.2$  dex (given their excess sSFR relative to MS galaxies) based on the empirical model of Sargent et al. (2014), shown in Figure 3b.

These results may be indicative of a more continuous range in SFE as opposed to the notion of a second mode of star-formation, distinct from that of MS galaxies, operating at higher efficiency (Daddi et al. 2010b; Genzel et al. 2010, 2015). However, any statement on differences in SFE requires a factor  $\alpha_{CO}$  to convert CO luminosity to molecular  $H_2$  gas mass (as further addressed below). Even with continuity in these parameters, there could still exist an underlying bi-modal physical framework for star formation as demonstrated with empirical models shown in Figure 3b and fully explained in Sargent et al. (2014).

### 3.2. Gas masses, $\alpha_{CO}$ , and SFE

With PACS-819 and PACS-830 having marginally resolved CO emission, we can estimate the total gas mass using the dynamical mass method (e.g., Tan et al. 2014). The dynamical mass ( $M_{dyn}$ ) within the half-light radius ( $r_{1/2}$ ) is given for the spherically symmetric case by:

$$M_{dyn}(r < r_{1/2}) \simeq \frac{5\sigma^2 r_{1/2}}{G} \quad (1)$$

where  $\sigma = \Delta v_{CO}/2.35$  is the velocity dispersion,  $\Delta v_{CO}$  is the line width - FWHM, and  $G$  is the gravitational constant. The gas mass is then derived by subtracting from the dynamical mass half of the stellar mass and a dark matter component ( $M_{DM} = 0.25 \times M_{dyn}$ ; Daddi et al. 2010a) as follows.

$$M_{dyn} = 0.5 \times (M_* + M_{gas}) + M_{DM}(r < r_{1/2}). \quad (2)$$

We estimate the gas mass for PACS-819 (PACS-830) to be  $2.0$  ( $6.2$ )  $\times 10^{10} M_\odot$ , based on their half-light radii, respectively  $1.4$  kpc and  $4.1$  kpc and velocity dispersion  $\sigma$ , respectively  $168.0$   $\text{km s}^{-1}$  and  $148.7$   $\text{km s}^{-1}$ , that corresponds to a gas fraction ( $f_{gas} = M_{gas}/(M_{gas} + M_*)$ ) of  $0.34$  ( $0.46$ ). Based on these values, we estimate  $\alpha_{CO} \simeq 0.6$  for PACS-819 and  $1.6$  for PACS-830, both not far from those found for the high-redshift submillimeter galaxies in the proto-cluster GN20 (Tan et al. 2014) and consistent with lower conversion factors for galaxies in mergers (Narayanan et al. 2011) as compared to isolated disk galaxies (see also Genzel et al. 2015).

We can further estimate the  $H_2$  gas masses from the CO line luminosity for the galaxies with unresolved CO emission using the average ( $\alpha_{CO} = 1.1 M_\odot / \text{K km s}^{-1} \text{pc}^{-2}$ ) value of the two estimates of  $\alpha_{CO}$  given above which is in very close agreement to that found for local nuclear starbursts ( $\alpha_{CO} = 0.8$ ; Downes & Solomon 1998). These estimates are simply approximations since the true molecular gas mass may be higher. Based on these conversion factors, the gas masses of our galaxies are typically in the range  $\sim (1.3 - 6.2) \times 10^{10} M_\odot$ . This results in gas fractions ( $f_{gas} = M_{gas}/(M_{gas} + M_*)$ ) between 28 and 52% (see Table 1 for individual estimates), similar to those of MS galaxies at these redshifts (Tacconi et al.

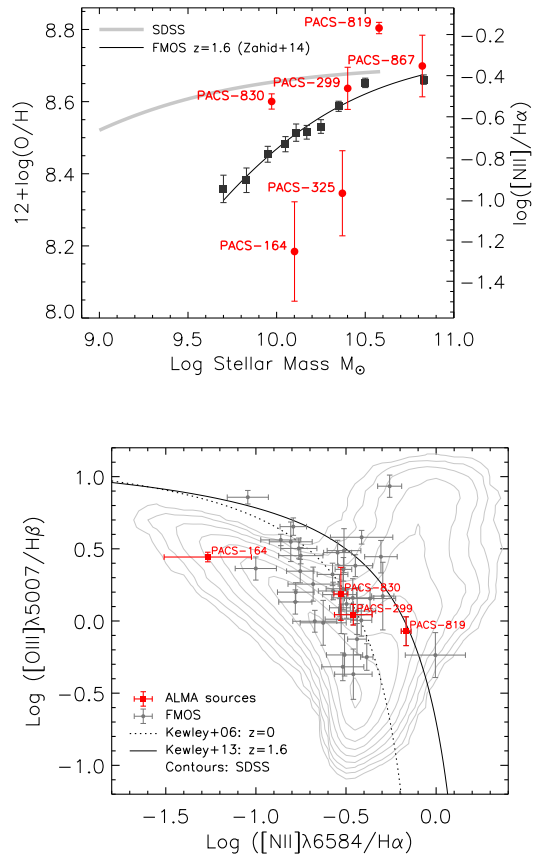


**Figure 4.** Rest-frame emission line ratios from FMOS-COSMOS: (a) Mass - metallicity relation of our high- $z$  starburst sample (red points). For comparison, we plot the M-Z relation, based on  $[NII]\lambda 6585/H\alpha$ , at low redshift from SDSS (grey line) and at  $z \sim 1.6$  (black squares) using average spectra (Zahid et al. 2014). (b) BPT diagram at  $z \sim 1.6$  (Kartaltepe et al. 2015) with CO sample as indicated. Individual measurements, shown in grey, represent galaxies from our larger sBzK sample (Silverman et al. 2014). Contours denote the region of parameter space spanned by low-redshift star-forming galaxies in SDSS. Theoretical curves separating star-forming galaxies and AGN (that evolve with redshift) are given. All data points have  $\pm 1\sigma$  errors.

2013; Béthermin et al. 2015) and inline with cosmological galaxy formation models (Narayanan et al. 2012).

Based on these results, an increase in the SFE is likely responsible for their elevation above the MS. In Figure 3c, we illustrate this scenario by plotting the gas depletion timescale ( $\tau_{del} \equiv SFE^{-1}$ ; units Gyr) as a function of SFR. As described above, the lower CO luminosities at a given  $L_{TIR}$ , compared to MS galaxies, are indicative of a lower gas mass hence shorter gas depletion timescales and higher SFEs, in agreement with previous studies (Genzel et al. 2010; Daddi et al. 2010b). Despite the remaining uncertainties on the assumptions used to derive  $H_2$  masses, we see evidence that starbursts in our sample have less extreme SFEs than those measured for the local ULIRGs and strongest starbursts at high- $z$ .

As a final check, we can assess whether the values of  $\alpha_{CO}$  derived above are appropriate for our starbursts by using the metallicity of the ISM as a proxy, given that it is well established that  $\alpha_{CO}$  is anti-correlated with metallicity (e.g., Schrubba et al. 2012; Genzel et al. 2012). In Figure 4, we show the mass-metallicity relation at  $z \sim 1.6$

(Zahid et al. 2014) based on  $[\text{NII}]\lambda 6585/\text{H}\alpha$ , with data for our sample over-plotted in red. We find that 4 out of 6 galaxies (having errors  $< \pm 0.2$  on the ratio) have high metallicities, similar to those of local galaxies. Therefore, our derived values of  $\alpha_{\text{CO}}$  are consistent with local galaxies of a similar metallicity, although with the caveat that we are not certain whether the metallicity of the line-emitting gas is representative of the molecular gas producing the CO emission.

We also examine whether AGN photo-ionization is contributing to the high  $[\text{NII}]/\text{H}\alpha$  ratios seen in some of our galaxies. Figure 4b, shows the FMOS-COSMOS version of the BPT diagram at  $z \sim 1.6$ . Four galaxies have all key diagnostic lines detected by FMOS. None of our galaxies fall in the region where strong AGN contribution is expected, above the line separating AGN from star-forming galaxies at  $z \sim 1.6$  (Kewley et al. 2013). While PACS-819 approaches this line, it is not detected in X-rays with *Chandra*. Nevertheless, we cannot rule out the presence of a low-to-moderate luminosity AGN, especially because its strong  $[\text{NII}]$  emission also drives this galaxy above the local MZ relation. For reference, in Figure 4b we plot the data for the larger star-forming galaxy population from FMOS-COSMOS (grey data points; Silverman et al. 2014), with further discussion in Kartaltepe et al. (2015). It is worth highlighting that both PACS-830 and PACS-299 fall within the locus of the star-forming population, clearly offset towards a higher ionization state of the ISM compared to local galaxies (Steidel et al. 2014; Kartaltepe et al. 2015).

#### 4. CONCLUDING REMARKS

Our observations of the molecular CO gas content of seven galaxies well-above the MS at  $z \sim 1.6$  with ALMA in Cycle 1 and IRAM/PdBI establish an offset in the  $L'_{\text{CO}} - L_{\text{TIR}}$  relation for starbursts at high redshift, compared to MS galaxies, although less than expected from previous studies mainly at lower redshift. These results may be indicative of a continuous distribution in SFE at high redshift, as a function of distance from the star-forming MS, as opposed to a bi-modal distribution.

An appealing physical explanation for a decrease in the  $L'_{\text{CO}}/L_{\text{TIR}}$  ratio for galaxies well-above the MS is galaxy mergers that can lead to rapid gas compression hence effectively boosting star formation resulting in shorter gas depletion timescales. Several galaxies well-above the MS are indeed in a merger phase (Rodighiero et al. 2011; Wuyts et al. 2011). Within the present sample, hints of merging come from the presence of multiple UV/optical emitting regions (e.g., in PACS-819, PACS-830, PACS-867), even being in a kinematically-linked system (PACS-164).

We highlight that our study is the result of the broad multi-wavelength coverage of the COSMOS field to measure accurate stellar masses and SFRs, capitalizing on the infrared photometry with *Spitzer* and *Herschel*. Equally important, accurate spectroscopic redshifts provided by the FMOS-COSMOS survey have guaranteed that the location of the CO emission lines fall well within the ALMA and PdBI passbands. The availability of key diagnostic emission lines in the rest-frame optical band

enable us to further assess the ionization state and chemical enrichment of the ISM where we already see similarities with the inner regions of local ULIRGs (Rich et al. 2014). We concede that a larger sample of  $z \sim 1.6$  starburst galaxies is needed to conclusively distinguish between the aforementioned scenarios. As shown in Figure 1, there are many potential targets within the redshift range 1.4 to 1.7 that can be observed by both FMOS and ALMA.

#### REFERENCES

- B ethermin, M., Daddi, E., Magdis, G., et al. 2015, * *, 573, A113  
 Bouch e, N., Dekel, A., Genzel, R., et al. 2010, *ApJ*, 718, 1001  
 Bruzual, G., & Charlot, S. 2003, *MNRAS*, 344, 1000  
 Daddi, E., Dickinson, M., Morrison, G. et al. 2007, *ApJ*, 670, 156  
 Daddi, E., Bournaud, F., Walter, F. et al. 2010a, *ApJ*, 713, 686  
 Daddi, E., Elbaz, D., Walter, F. et al. 2010b, *ApJ*, 714, L118  
 Downes, D., & Solomon, P. M. 1998, *ApJ*, 507, 615  
 Elbaz, D., Daddi, E., Le Borgne, D. et al. 2007, * *, 468, 33  
 Genzel, R., Tacconi, L. J., Gracia-Carpio, J., et al. 2010, *MNRAS*, 407, 2091  
 Genzel, R., Tacconi, L. J., Combes, F., et al. 2012, *ApJ*, 746, 69  
 Genzel, R., Tacconi, L. J., Lutz, D., et al. 2015, *ApJ*, 800, 20  
 Kartaltepe, J. Sanders, D. B., Silverman, J. D. et al., *ApJ*, in press  
 Kashino, D., Silverman, J., Rodighiero, G. et al. *ApJ*, 777, L8  
 Kewley, L., Dopita, M., Leitherer, C., et al. 2013, *ApJ*, 774, 100  
 Lilly, S. J., Carollo, C. M., Pipino, A., 2013, *ApJ*, 772, 119  
 Lilly, S. J., Le F evre, O., Renzini, A., et al. 2013, *ApJ*, 772, 119  
 Madau, P., & Dickinson, M. 2014, *ARA&A*, 52, 415  
 Magdis, G. E., Daddi, E., B ethermin, M. 2012, *ApJ*, 760, 6  
 Narayanan, D., Krumholz, M., Ostriker, E. C., & Hernquist, L. 2011, *MNRAS*, 418, 664  
 Narayanan, D., Bothwell, M., & Dav e, R. 2012, *MNRAS*, 426, 1178  
 Noeske, K., Weiner, B. J., Faber, S. M. et al. 2007, *ApJ*, 660, L43  
 Rich, M., Kewley, L., Dopita, M. 2014, *ApJ*, 781, L12  
 Rodighiero, G., Daddi, E., Baronchelli, I. et al. 2011, *ApJ*, 739, L40  
 Sanders, D. B. & Mirabel, I. F. 1996, *ARA&A*, 34, 749  
 Santini, P., Maiolino, R., Magnelli, B. 2014, * *, 562, A30  
 Sargent, M. T., Daddi, E., B ethermin, M. et al. 2014, *ApJ*, 793, 19  
 Schinnerer, E., Sargent, M. T., Bondi, M. et al. 2010, *ApJS*, 188, 384  
 Schrubba, A., Leroy, A. K., Walter, F. et al. 2012, *AJ*, 143, 138  
 Scoville, N. Z., Sanders, D. B., Sargent, A. I. et al. 1989, *ApJ*, 345, L25  
 Scoville, N. Z., Aussel, H., Sheth, K. et al. 2014, *ApJ*, 783, 84  
 Silverman, J. D., Kashino, D., Arimoto, N. et al. 2014, *arXiv:1409.0447*  
 Solomon, P. M., Downes, D., Radford, S. J. E., & Barrett, J. W. 1997, *ApJ*, 478, 144  
 Speagle, J. S., Steinhardt, C. L., Capak, P. L., Silverman, J. D. 2014, *ApJS*, 214, 15  
 Steidel, C. C., Rudie, G. C., Strom, A. L. et al. 2014, *ApJ*, 795, 165  
 Swinbank, A. M., Simpson, J. M., Smail, I. et al. 2014, *MNRAS*, 438, 1267  
 Tacconi, L., Genzel, R., Neri, R., et al. 2010, *Nature*, 463, 781  
 Tacconi, L., Neri, R., Genzel, R., et al. 2013, *ApJ*, 768, 74  
 Tan, Q., Daddi, E., Magdis, G. et al. 2014, * *, 569, A98  
 Whitaker, K. E., van Dokkum, P. G., Brammer, G. et al. 2012, *ApJ*, 754, L29  
 Wuyts, S., F orster Schreiber, N. M., van der Wel, A. et al. 2011, *ApJ*, 742, 96  
 Zahid, H. J., Kashino, D., Silverman, J. D., et al. 2014, *ApJ*, 792, 75